Engineering Analysis with Boundary Elements 121 (2020) 21–30

Contents lists available at ScienceDirect

Engineering Analysis with Boundary Elements

journal homepage: www.elsevier.com/locate/enganabound

A new implementation of DRM with dual interpolation boundary face method for Poisson equation

Rui He[a], Jianming Zhang[a,*], Suliman[b], Le Yang[a], Weicheng Lin[a]

[a] State Key Laboratory of Advanced Design and Manufacturing for Vehicle Body, College of Mechanical and Vehicle Engineering, Hunan University, Changsha 410082, China

[b] School of Mathematics and Statistics, Central South University, Changsha 410083, China

ARTICLE INFO

Keywords:
Dual reciprocity method
Radial basis functions
Dual interpolation boundary face method
Hermite-type approximation
Poisson equation

ABSTRACT

We present a new numerical algorithm combining the dual reciprocity method with the dual interpolation boundary face method for solving the two-dimensional Poisson equations. In this new combined approach, the boundary physical variables and particular solutions are approximated by dual interpolation elements which include source and virtual points. Additionally, this algorithm is implemented by employing the augmented thin plate spline interpolation function to approximate non-homogeneous term and the Hermite-type moving-least-square approximation to approximate physical variables for virtual nodes. Compared with the traditional dual reciprocity boundary element method, this combined method possesses higher accuracy and efficiency and is better suited for structures with small feature sizes. Several numerical examples are given to illustrate the superiority of the proposed method for solving Poisson equations.

1. Introduction

The boundary element method (BEM) is a well-established numerical technique for solving various scientific and engineering problems [1–5]. In early times, the BEM applications always needed a requirement that a fundamental solution for the problem had to be available. Otherwise, domain integrals existed in the formulation of the boundary integral equation and the internal cells had to be required [6]. In order to avoid the problems mentioned above, Nardini and Brebbia [7] firstly introduced the dual reciprocity method (DRM) which was also called as the dual reciprocity boundary element method (DRBEM), and this method has been developed by many researchers to solve various physical problems [8–10].

The DRM became a popular method for extending the boundary element method to solve non-homogeneous partial differential equations, often referred to as Poisson equations. In this method, the non-homogeneous term is approximated by a set of radial basis functions (RBFs) defined at the specified boundary and internal nodes. There are several suitable RBFs to be used in DRM. The adhoc choice $1+r$ proposed by Brebbia and Nardini was almost exclusively used in the early literature. Then, following the articles by Golberg and Chen [11], the thin plate spline (TPS), augmented thin plate spline (ATPS) and multiquadrics (MQs) [12, 13] were increasingly used. Furthermore, the other choices were the Gaussians and higher order splines [14]. However, for a large number of interpolation points, the resulting matrixes for interpolation obtained by those classic functions were dense and highly ill-conditioned [15]. Thus, the compactly supported radial basis functions (CS-RBFs) were proposed [16]. The accurate approximation by RBFs of non-homogeneous term improves the accuracy and efficiency of the DRM. Moreover, if we use the discontinuous elements to implement the DRBEM, many numbers of elements will be required to obtain satisfactory results, because of the low interpolation accuracy of discontinuous elements.

The recently proposed dual interpolation boundary face method (DiBFM) [17–21] has been demonstrated the higher accuracy and efficiency, compared with the traditional boundary element method. Those advantages are mainly based on two reasons: (i) Compared with conventional discontinuous elements, the dual interpolation elements in DiBFM improve the interpolation accuracy by two orders; (ii) The DiBFM eliminated geometry error since the integrand quantities are calculated directly from the curves rather than from elements [22]. Moreover, the method used in the second-layer interpolation plays an important role in the DiBFM. In the recent DiBFM literatures, there are three kinds of second-layer interpolation methods, as referred to expending element method [17], moving least-squares (MLS) approximation [18] and Hermite-type moving least-squares (HMLS) approximation [20, 21]. So this provides a way to apply the dual interpolation method to implement the DRM.

In this paper, we present a new numerical approach by combining the DRM with the dual interpolation boundary face method for solving

* Corresponding author.
E-mail address: zhangjm@hnu.edu.cn (J. Zhang).

https://doi.org/10.1016/j.enganabound.2020.09.004
Received 6 March 2020; Received in revised form 24 July 2020; Accepted 2 September 2020
Available online 15 September 2020

Poisson equations. In this new combined algorithm, the boundary physical variables and particular solutions are approximated by dual interpolation elements. In addition, it should be mentioned that we use the ATPS interpolation function to approximate the inhomogeneous term for its advantages pointed in literature [13]: (i) the interpolation matrix is always non-singular; (ii) under uniform mesh refinement the convergence rate is of order (h^4), h being the mesh spacing; (iii) the interpolation is exact for a constant or a linear function of the position variables. Furthermore, the HMLS approximation is employed to approximate the physical variables for virtual nodes, since it is suited to solve for structures having small feature sizes, such as short edges and small chamfers [20, 21]. Therefore, compared with the traditional DRBEM, this new combined method largely improves the accuracy and efficiency and is also suited for structures with small feature sizes.

The article is divided into six Sections. In Section 2, we introduce the dual reciprocity method for the Poisson equation and radial basis functions in DRM. In Section 3, we describe the dual interpolation method with Hermite-type moving least-squares approximation. In Section 4, we present the DRM combined with dual interpolation boundary face method for Poisson equation. In Section 5, the results of several numerical examples are given to illustrate the superiority of the proposed method. We close with some discussions and conclusions.

2. The dual reciprocity method for the Poisson equation

In this section, we introduce the dual reciprocity method for the Poisson equation. Considering the following equation:

$$\begin{aligned} \nabla^2 u &= b(x,y), && \forall \mathbf{x} \in \Omega \\ u &= \bar{u}, && \forall \mathbf{x} \in \Gamma_u, \\ q &= \frac{\partial u}{\partial n} = \bar{q}, && \forall \mathbf{x} \in \Gamma_q \end{aligned} \tag{1}$$

where the domain Ω is enclosed by the boundary $\Gamma = \Gamma_u + \Gamma_q$, $b(x, y)$ is the source term assumed to be a known function, $\bar{u}$ and $\bar{q}$ are the prescribed values of the potential and normal flux on the boundaries Γ_u and Γ_q, respectively, and n is the outward normal of the boundary Γ.

By applying the Green's integral formula, Eq. (1) can be transformed into the following integral form:

$$\begin{aligned} &c(P)u(P) + \int_\Gamma q^*(P,Q)u(Q)d\Gamma(Q) - \int_\Gamma u^*(P,Q)q(Q)d\Gamma(Q) \\ &= \int_\Omega u^*(P,q)b(q)d\Omega(q), \end{aligned} \tag{2}$$

where P and Q are the boundary source and field point, q is the inner field point, the constant $c(P)$ has value from 0 to 1, being equal to 1/2 for smooth boundaries and 1 for the internal source point, $u^*(P, Q)$ and $q^*(P, Q)$ are fundamental solutions of the Laplace equation, respectively. For the 2-D potential problems, $u^*(P, Q)$ and $q^*(P, Q)$ are given by:

$$u^*(P,Q) = \frac{1}{2\pi}\ln\left(\frac{1}{r(P,Q)}\right), \tag{3}$$

$$q^*(P,Q) = \frac{\partial u^*(P,Q)}{\partial n(Q)}, \tag{4}$$

where $r(P, Q)$ is the Euclidean distance between points P and Q.

2.1. The dual reciprocity boundary element method

The basic idea of DRM is to expand the source term b using the following approximation:

$$b \simeq \sum_{n=1}^{NR} \alpha_n f(\xi_n, q), \tag{5}$$

where $f(\xi_n,q)$ are the radial basis functions (RBFs) defined at fixed collocation point ξ_n, and α_n are a set of initially unknown coefficients, NR is the number of RBFs, respectively.

Table 1
Particular solutions corresponding to ATPS.

f	1	x	y	$r^2\ln r$
$\hat{u}_n$	$r^2/4$	$x^3/6$	$y^3/6$	$r^4(2\ln r - 1)/32$
$\hat{q}_n$	$\frac{1}{2}(r_x n_x + r_y n_y)$	$\frac{x^2}{2}n_x$	$\frac{y^2}{2}n_y$	$\frac{1}{16}r^2(r_x n_x + r_y n_y)(4\ln r - 1)$

where r_x and r_y are the projections of r on the x and y axes, n_x and n_y are direction cosines refer to the outward normal at the boundary with respect to the x and y axes, respectively.

Applying the RBFs approximation to the source term b and using the Green's formula again, Eq. (2) can be recast in terms of a series of boundary integrals as follows:

$$\begin{aligned} &c(P)u(P) + \int_\Gamma q^*(P,Q)u(Q)d\Gamma(Q) - \int_\Gamma u^*(P,Q)q(Q)d\Gamma(Q) \\ &= \sum_{n=1}^{NR} \alpha_n \left(c(P)\hat{u}_n(P) + \int_\Gamma q^*(P,Q)\hat{u}_n(Q)d\Gamma(Q) - \int_\Gamma u^*(P,Q)\hat{q}_n(Q)d\Gamma(Q)\right) \end{aligned} \tag{6}$$

where $\hat{u}_n$ and $\hat{q}_n$ are the particular solutions according to the radial basis functions $f(\xi_n,q)$.

2.2. The radial basis functions in DRM

There are several choices in selecting RBF, such as the linear function $1 + r$, thin plate spline (TPS) $r^2\ln r$, Gaussian e^{-r^2/β^2} and multiquadrics $\beta^2 + r^2$, where β is a constant parameter. We defined the numbers of boundary and domain collocation points as N_B and N_D in the above RBFs, respectively, with NR=NB+ND. In this paper, we choose the augmented thin plate splines (ATPS), which combined thin plate splines and linear functions, to perform the DRM. Thus, NR=NB+ND+3, the interpolation matrix is always non-singular and the approximation of source term b is formulated as

$$b \simeq \sum_{n=1}^{NB+ND} \alpha_n r^2(\xi_n, q)\ln r(\xi_n, q) + \alpha_{NB+ND+1} + \alpha_{NB+ND+2}x + \alpha_{NB+ND+3}y, \tag{7}$$

To obtain all unknown coefficients, three additional equations are required

$$\sum_{n=1}^{NB+ND} \alpha_n = \sum_{n=1}^{NB+ND} \alpha_n x_n = \sum_{n=1}^{NB+ND} \alpha_n y_n = 0, \tag{8}$$

where (x_n,y_n) is the coordinates of the n^{th} collocation point. The method is available in [13] to obtain all unknown interpolation coefficientsα_n, n=1 to NR.

The corresponding particular solutions are given as follows:
Table 1

3. Dual interpolation method with HMLS approximation

In this section, we introduce the first-layer interpolation for boundary variables and the second-layer interpolation for virtual nodes. In our implementation, the HMLS approximation is applied, because of its high accuracy and superiority in disposing the structures with small feature sizes.

3.1. First-layer interpolation for boundary variables

The 2D dual interpolation element shown in Fig. 1 is composed of source (s_i) and virtual (v_i) nodes. In Eq. (6), it should be highlighted that not only the physical variables u and q but also the particular solutions $\hat{u}_n$ and $\hat{q}_n$ on the boundary are approximated by dual interpolation element. Thus, the above boundary variables are approximated by first-layer interpolation as follows:

$$u(\xi) = \sum_{\alpha=1}^{n_\alpha} N_\alpha^S(\xi)u(Q_\alpha^s) + \sum_{\beta=1}^{n_\beta} N_\beta^V(\xi)u(Q_\beta^V), \tag{9}$$

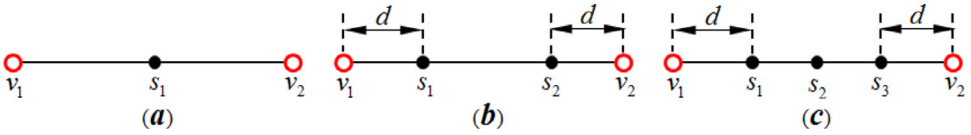

Fig. 1. The 2D dual interpolation elements: (a) S1, (b) S2, and (c) S3.

$$q(\xi) = \sum_{\alpha=1}^{n_\alpha} N_\alpha^s(\xi) q(Q_\alpha^s) + \sum_{\beta=1}^{n_\beta} N_\beta^v(\xi) q(Q_\beta^v), \tag{10}$$

$$\hat{u}_n(\xi) = \sum_{\alpha=1}^{n_\alpha} N_\alpha^s(\xi) \hat{u}_n(Q_\alpha^s) + \sum_{\beta=1}^{n_\beta} N_\beta^v(\xi) \hat{u}_n(Q_\beta^v), \tag{11}$$

$$\hat{q}_n(\xi) = \sum_{\alpha=1}^{n_\alpha} N_\alpha^s(\xi) \hat{q}_n(Q_\alpha^s) + \sum_{\beta=1}^{n_\beta} N_\beta^v(\xi) \hat{q}_n(Q_\beta^v), \tag{12}$$

where n_α and n_β are the number of source and virtual nodes in the dual interpolation element, $N_\alpha^s(\xi)$, $u(Q_\alpha^s)$, $q(Q_\alpha^s)$, $\hat{u}_n(Q_\alpha^s)$ and $\hat{q}_n(Q_\alpha^s)$ are the shape function, potential, normal flux and the values of n^{th} particular solutions of the α^{th} source node in the dual interpolation element, and $N_\beta^v(\xi)$, $u(Q_\beta^v)$, $q(Q_\beta^v)$, $\hat{u}_n(Q_\beta^v)$ and $\hat{q}_n(Q_\beta^v)$ are the shape function, potential, normal flux and the values of n^{th} particular solutions of the β^{th} virtual node in the dual interpolation element, respectively.

3.2. Second-layer interpolation for virtual nodes

The potentials u and normal fluxes q of virtual points in Eq. (9) and (10) are approximated by those of source points. Here, we employ the HMLS approximation to obtain the u and q of virtual points. It should be noted that the particular solutions $\hat{u}_n$ and $\hat{q}_n$ of virtual points are known. Thus, only u and q of virtual points are approximated as follows:

$$u(Q_\beta^v) = \sum_{I=1}^{N_P} \phi_I^{uu} u(Q_I^s) + \sum_{I=1}^{N_P} \phi_I^{uq} q(Q_I^s), \tag{13}$$

$$q(Q_\beta^v) = \sum_{I=1}^{N_P} \phi_I^{qu} u(Q_I^s) + \sum_{I=1}^{N_P} \phi_I^{qq} q(Q_I^s), \tag{14}$$

where N_p is the number of source nodes located in the influence domain of the virtual node Q_β^v, $u(Q_I^s)$ and $q(Q_I^s)$ are the potential and normal flux of source node Q_I^s, $\phi_I^{uu}(x^v, y^v)$, $\phi_I^{uq}(x^v, y^v, n^v)$, $\phi_I^{qu}(x^v, y^v)$, and $\phi_I^{qq}(x^v, y^v, n^v)$ are the HMLS interpolation shape functions, which are available in literatures [20] and [23].

4. DRM with dual interpolation boundary face method for Poisson equation

In this section, we will employ the dual interpolation elements to discretize the boundary integral equation formulated by Eq. (6), and use the HMLS approximation to condense the degrees of freedom for virtual nodes.

4.1. Discretization of the BIE by dual interpolation elements

In the following sections, the symbols *NE, NS, NV*, and *NM* denote the numbers of elements, source nodes, virtual nodes and field nodes, respectively. In our method, the boundary integral equations are only collocated at the source nodes. Therefore, the discretized form of Eq. (6) is as follows:

$$\sum_{j=1}^{NE}\sum_{k=1}^{M^j} h_{ij}^k u_j^k - \sum_{j=1}^{NE}\sum_{k=1}^{M^j} g_{ij}^k q_j^k = \sum_{n=1}^{NR} \alpha_n \left(\sum_{j=1}^{NE}\sum_{k=1}^{M^j} h_{ij}^k \hat{u}_{jn}^k - \sum_{j=1}^{NE}\sum_{k=1}^{M^j} g_{ij}^k \hat{q}_{jn}^k \right), \quad i = 1, 2, \ldots, NS, \tag{15}$$

with

$$h_{ij}^k = \int_{\Gamma_j} q^* N_j^k d\Gamma + \frac{1}{2}\delta_{ij}^k, \tag{16}$$

$$g_{ij}^k = \int_{\Gamma_j} u^* N_j^k d\Gamma, \tag{17}$$

and

$$\delta_{ij}^k = \begin{cases} 1, & \text{if the } i^{\text{th}} \text{source node is the } k^{\text{th}} \text{ source node in the } j^{\text{th}} \text{ element} \\ 0 \end{cases}, \tag{18}$$

where u_j^k and q_j^k are the potential and the normal flux of the k^{th} interpolation node of the j^{th} element, $\hat{u}_{jn}^k$ and $\hat{q}_{jn}^k$ are the values of n^{th} particular solutions at the k^{th} interpolation node of the j^{th} element, respectively, M^j denotes the number of interpolation nodes of the j^{th} element, and N_j^k represents the shape function of the first-layer interpolation for the k^{th} interpolation node of the j^{th} element. Eq. (15) can be given in the matrix form

$$\mathbf{Hu} - \mathbf{Gq} = \sum_{n=1}^{NR} \alpha_n (\mathbf{H}\hat{\mathbf{u}}_n - \mathbf{G}\hat{\mathbf{q}}_n), \tag{19}$$

where $\mathbf{H}$ and $\mathbf{G}$ are $NS \times NM$ coefficient matrices, $\mathbf{u}$ and $\mathbf{q}$ are $NM \times 1$ vectors containing the potentials and the normal fluxes of all field nodes, $\hat{\mathbf{u}}_n$ and $\hat{\mathbf{q}}_n$ are $NM \times 1$ vectors corresponding to the n^{th} particular solution, respectively. As we can see, Eq. (19) is unsolvable since the coefficient matrices are not square. We will employ the second-layer interpolation to make it solvable, which will be described in detail in the next section.

4.2. Condensation of degrees of freedom for virtual nodes by HMLS approximation

Differentiating the source and virtual nodes in Eq. (19), we obtain:

$$\begin{bmatrix} \mathbf{H}^{ss} & \mathbf{H}^{sv} \end{bmatrix} \begin{Bmatrix} \mathbf{u}^s \\ \mathbf{u}^v \end{Bmatrix} - \begin{bmatrix} \mathbf{G}^{ss} & \mathbf{G}^{sv} \end{bmatrix} \begin{Bmatrix} \mathbf{q}^s \\ \mathbf{q}^v \end{Bmatrix} = \sum_{n=1}^{NR} \alpha_n \left(\begin{bmatrix} \mathbf{H}^{ss} & \mathbf{H}^{sv} \end{bmatrix} \begin{Bmatrix} \hat{\mathbf{u}}_n^s \\ \hat{\mathbf{u}}_n^v \end{Bmatrix} - \begin{bmatrix} \mathbf{G}^{ss} & \mathbf{G}^{sv} \end{bmatrix} \begin{Bmatrix} \hat{\mathbf{q}}_n^s \\ \hat{\mathbf{q}}_n^v \end{Bmatrix} \right), \tag{20}$$

where $\mathbf{u}^s$ and $\mathbf{q}^s$ are the $NS \times 1$ potential and normal flux vectors for the source nodes, $\mathbf{u}^v$ and $\mathbf{q}^v$ are the $NV \times 1$ vectors corresponding to the virtual nodes, $\hat{\mathbf{u}}_n^s$, $\hat{\mathbf{q}}_n^s$, $\hat{\mathbf{u}}_n^v$ and $\hat{\mathbf{q}}_n^v$ are the n^{th} particular solution vectors for the source and virtual nodes, and $\mathbf{H}^{ss}$, $\mathbf{G}^{ss}$, $\mathbf{H}^{sv}$, and $\mathbf{G}^{sv}$ are the $NS \times NS$, $NS \times NS$, $NS \times NV$, $NS \times NV$ coefficient matrices, respectively.

First, we handle the left-side of Eq. (20). The vectors $\mathbf{u}^v$ and $\mathbf{q}^v$ can be recast according to the boundary condition:

$$\mathbf{u}^v = \bar{\mathbf{u}}^v + \widetilde{\mathbf{u}}^v, \tag{21}$$

$$\mathbf{q}^v = \bar{\mathbf{q}}^v + \widetilde{\mathbf{q}}^v, \tag{22}$$

where $\bar{\mathbf{u}}^v$, $\widetilde{\mathbf{u}}^v$, $\bar{\mathbf{q}}^v$, and $\widetilde{\mathbf{q}}^v$ are the known and unknown potentials and normal fluxes of the virtual nodes, respectively.

Each unknown potential and normal flux in $\widetilde{\mathbf{u}}^v$ and $\widetilde{\mathbf{q}}^v$ can be approximated using HMLS approximation defined by Eqs. (13) and (14). As a result, $\widetilde{\mathbf{u}}^v$ and $\widetilde{\mathbf{q}}^v$ can be expressed as follows:

$$\widetilde{\mathbf{u}}^v = \mathbf{\Phi}_{uu}^{vs}\mathbf{u}^s + \mathbf{\Phi}_{uq}^{vs}\mathbf{q}^s, \tag{23}$$

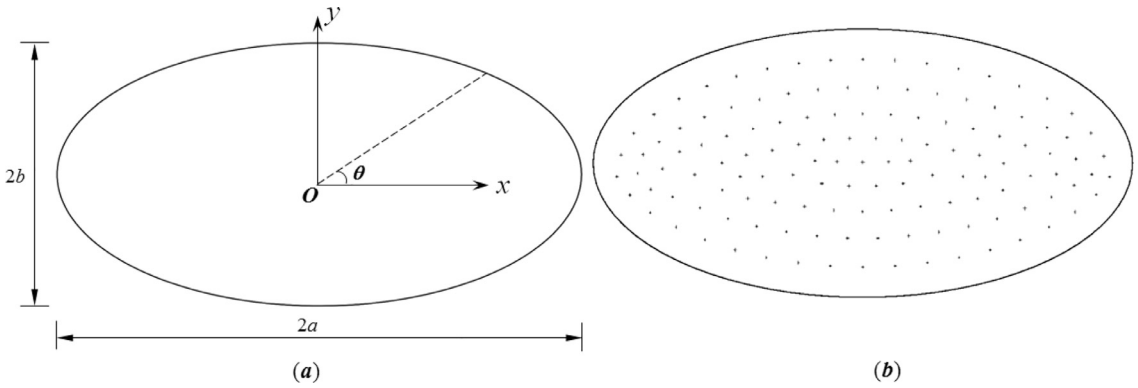

Fig. 2. Poisson equation on an ellipse: (a) geometric model and (b) the distribution of inner nodes.

$$\widehat{\mathbf{q}}^{v} = \mathbf{\Phi}_{qu}^{vs}\mathbf{u}^{s} + \mathbf{\Phi}_{qq}^{vs}\mathbf{q}^{s}, \tag{24}$$

where $\mathbf{\Phi}_{uu}^{vs}$, $\mathbf{\Phi}_{uq}^{vs}$, $\mathbf{\Phi}_{qu}^{vs}$, and $\mathbf{\Phi}_{qq}^{vs}$ are shape function matrices obtained by the HMLS approximation (section 3.2).

Combining Eqs. (20)—(24), we can obtain:

$$\mathbf{H}^{s}\mathbf{u}^{s} - \mathbf{G}^{s}\mathbf{q}^{s} - \mathbf{b}^{v} = \sum_{n=1}^{NR} \alpha_n \left(\begin{bmatrix} \mathbf{H}^{ss} & \mathbf{H}^{sv} \end{bmatrix} \begin{Bmatrix} \hat{\mathbf{u}}_n^{s} \\ \hat{\mathbf{u}}_n^{v} \end{Bmatrix} - \begin{bmatrix} \mathbf{G}^{ss} & \mathbf{G}^{sv} \end{bmatrix} \begin{Bmatrix} \hat{\mathbf{q}}_n^{s} \\ \hat{\mathbf{q}}_n^{v} \end{Bmatrix} \right), \tag{25}$$

with

$$\mathbf{H}^{s} = \mathbf{H}^{ss} + \mathbf{H}^{sv}\mathbf{\Phi}_{uu}^{vs} - \mathbf{G}^{sv}\mathbf{\Phi}_{qu}^{vs}, \tag{26}$$

$$\mathbf{G}^{s} = \mathbf{G}^{ss} + \mathbf{G}^{sv}\mathbf{\Phi}_{qq}^{vs} - \mathbf{H}^{sv}\mathbf{\Phi}_{uq}^{vs}, \tag{27}$$

$$\mathbf{b}^{v} = -\mathbf{H}^{sv}\bar{\mathbf{u}}^{v} + \mathbf{G}^{sv}\bar{\mathbf{q}}^{v}. \tag{28}$$

Then, we arrange the right-side of Eq. (25). The vectors $\hat{\mathbf{u}}_n^{s}$, $\hat{\mathbf{q}}_n^{s}$, $\hat{\mathbf{u}}_n^{v}$ and $\hat{\mathbf{q}}_n^{v}$ are all evaluated by using the n^{th} particular solution. Thus, there is no need to use the second-layer interpolation to obtain $\hat{\mathbf{u}}_n^{v}$ and $\hat{\mathbf{q}}_n^{v}$. Expanding the right-side of Eq. (25) as follows

$$\sum_{n=1}^{NR} \alpha_n \left(\begin{bmatrix} \mathbf{H}^{ss} & \mathbf{H}^{sv} \end{bmatrix} \begin{Bmatrix} \hat{\mathbf{u}}_n^{s} \\ \hat{\mathbf{u}}_n^{v} \end{Bmatrix} - \begin{bmatrix} \mathbf{G}^{ss} & \mathbf{G}^{sv} \end{bmatrix} \begin{Bmatrix} \hat{\mathbf{q}}_n^{s} \\ \hat{\mathbf{q}}_n^{v} \end{Bmatrix} \right)$$
$$= \sum_{n=1}^{NR} \alpha_n (\mathbf{H}^{ss}\hat{\mathbf{u}}_n^{s} + \mathbf{H}^{sv}\hat{\mathbf{u}}_n^{v} - \mathbf{G}^{ss}\hat{\mathbf{q}}_n^{s} - \mathbf{G}^{sv}\hat{\mathbf{q}}_n^{v}). \tag{29}$$

If each of the vectors $\hat{\mathbf{u}}_n^{s}$, $\hat{\mathbf{u}}_n^{v}$, $\hat{\mathbf{q}}_n^{s}$ and $\hat{\mathbf{q}}_n^{v}$ is considered to be one column of the matrices $\hat{\mathbf{U}}^{s}$, $\hat{\mathbf{U}}^{v}$, $\hat{\mathbf{Q}}^{s}$ and $\hat{\mathbf{Q}}^{v}$, respectively, then Eq. (25) may be rewritten into

$$\mathbf{H}^{s}\mathbf{u}^{s} - \mathbf{G}^{s}\mathbf{q}^{s} - \mathbf{b}^{v} = (\mathbf{H}^{ss}\hat{\mathbf{U}}^{s} + \mathbf{H}^{sv}\hat{\mathbf{U}}^{v} - \mathbf{G}^{ss}\hat{\mathbf{Q}}^{s} - \mathbf{G}^{sv}\hat{\mathbf{Q}}^{v})\boldsymbol{\alpha}. \tag{30}$$

The right-hand side of Eq. (30) is thus a known vector. Writing this equation as

$$\mathbf{H}^{s}\mathbf{u}^{s} - \mathbf{G}^{s}\mathbf{q}^{s} = \mathbf{b}_0, \tag{31}$$

where

$$\mathbf{b}_0 = (\mathbf{H}^{ss}\hat{\mathbf{U}}^{s} + \mathbf{H}^{sv}\hat{\mathbf{U}}^{v} - \mathbf{G}^{ss}\hat{\mathbf{Q}}^{s} - \mathbf{G}^{sv}\hat{\mathbf{Q}}^{v})\boldsymbol{\alpha} + \mathbf{b}^{v}. \tag{32}$$

Finally, applying the boundary conditions to Eq. (31) results in the following form:

$$\begin{Bmatrix} \bar{\mathbf{H}}^{s} & \widehat{\mathbf{H}}^{s} \end{Bmatrix} \begin{Bmatrix} \bar{\mathbf{u}}^{s} \\ \widehat{\mathbf{u}}^{s} \end{Bmatrix} = \begin{Bmatrix} \bar{\mathbf{G}}^{s} & \widehat{\mathbf{G}}^{s} \end{Bmatrix} \begin{Bmatrix} \bar{\mathbf{q}}^{s} \\ \widehat{\mathbf{q}}^{s} \end{Bmatrix} + \mathbf{b}_0, \tag{33}$$

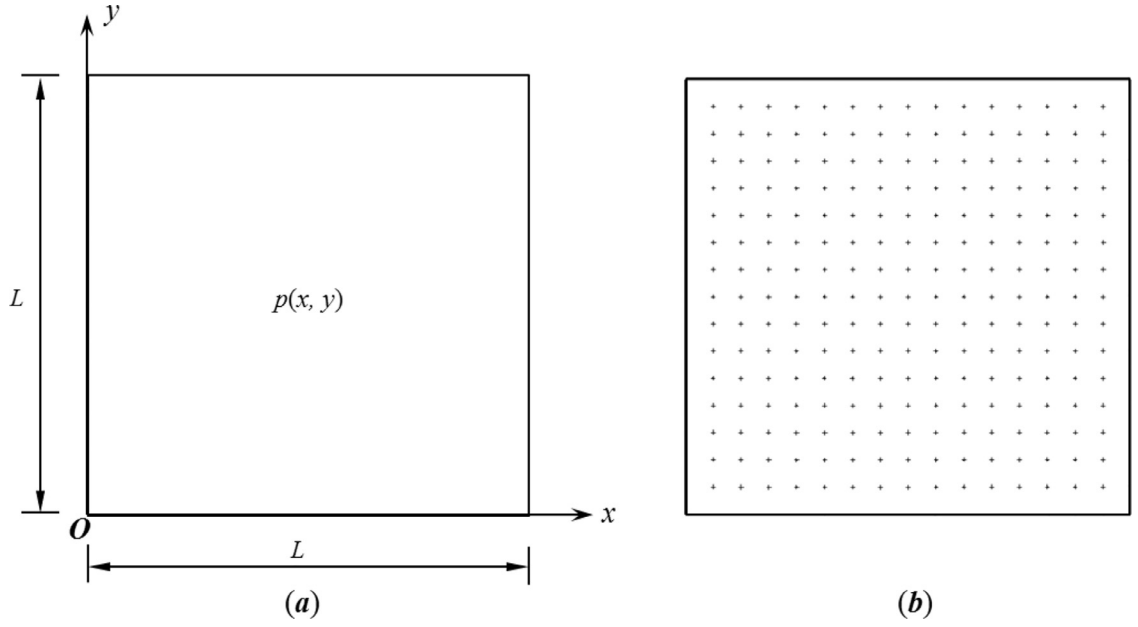

Fig. 7. Square membrane submitted to variable domain loading: (a) geometric features and (b) the distribution of internal nodes.

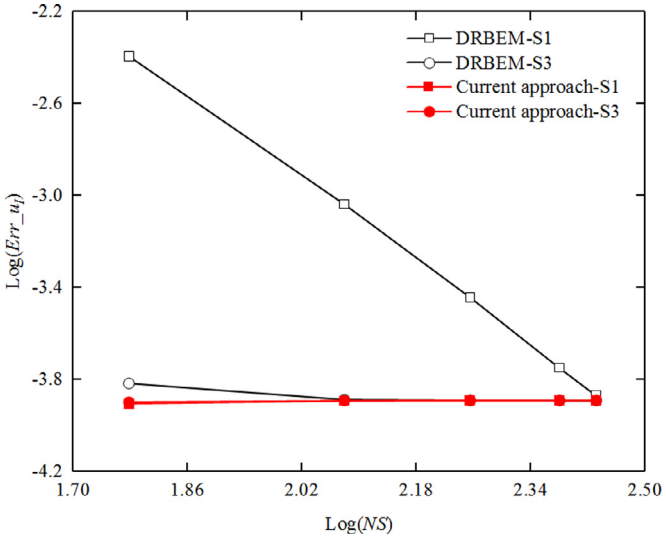

Fig. 3. Comparison of convergence for u_I in the first example.

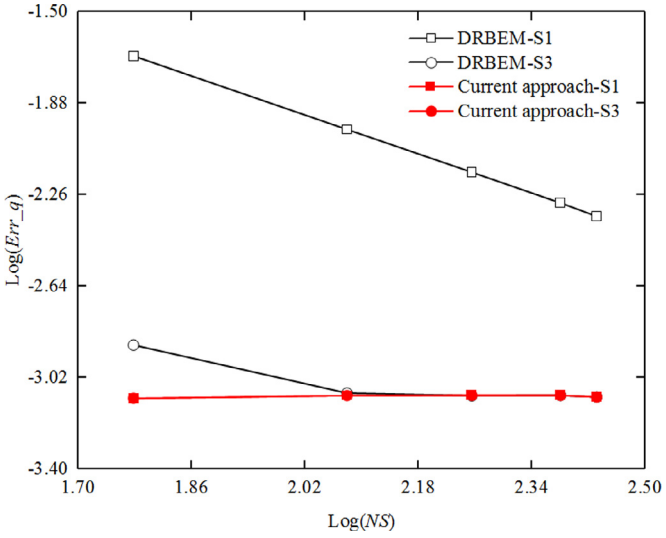

Fig. 4. Comparison of convergence for q in the first example.

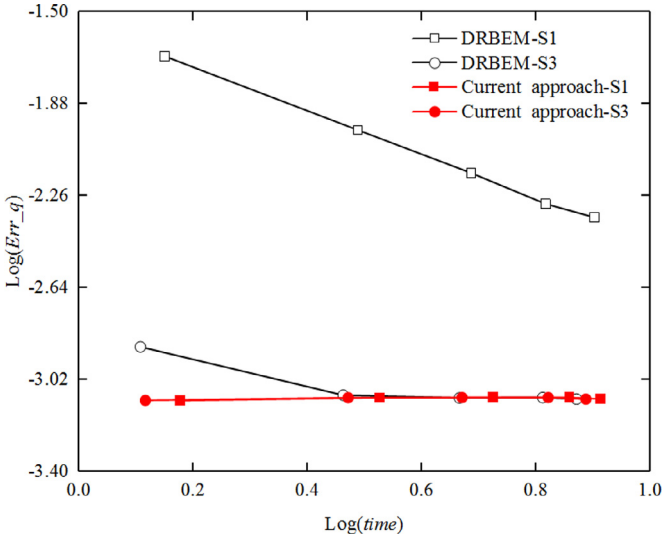

Fig. 5. Comparison of computational efficiency for q in the first example.

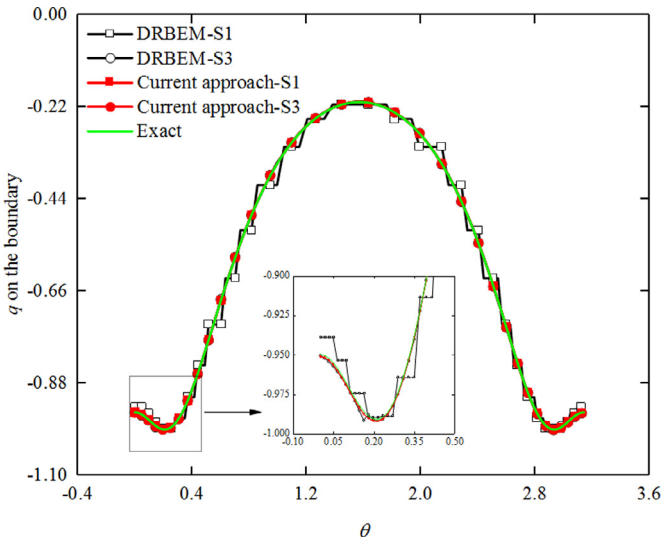

Fig. 6. Comparison of accuracy for q along the boundary for the first example.

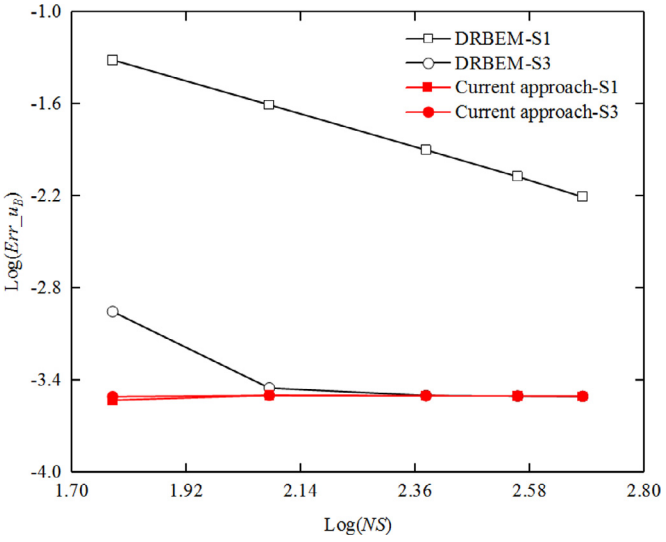

Fig. 8. Comparison of convergence for u_B in the second example.

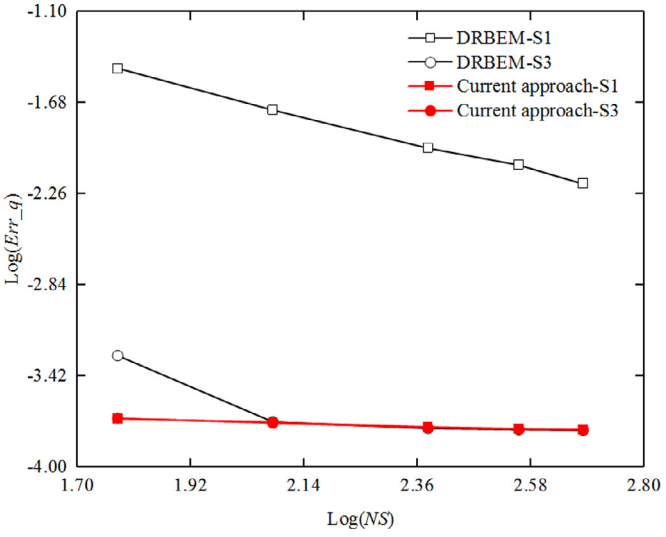

Fig. 9. Comparison of convergence for q in the second example.

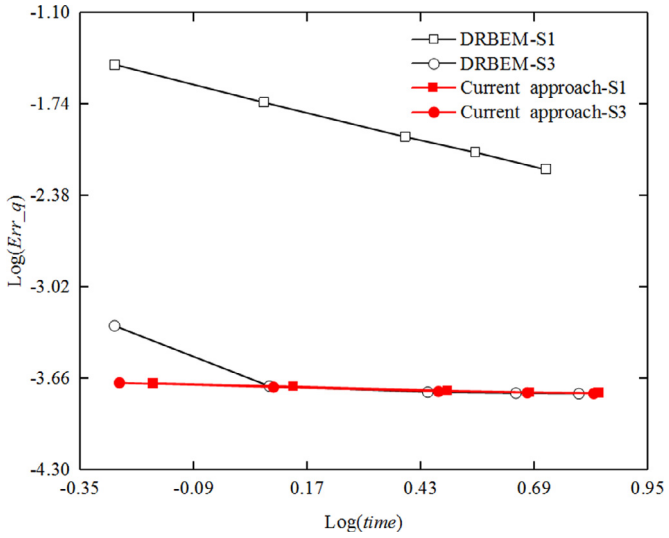

Fig. 10. Comparison of computational efficiency for q in the second example.

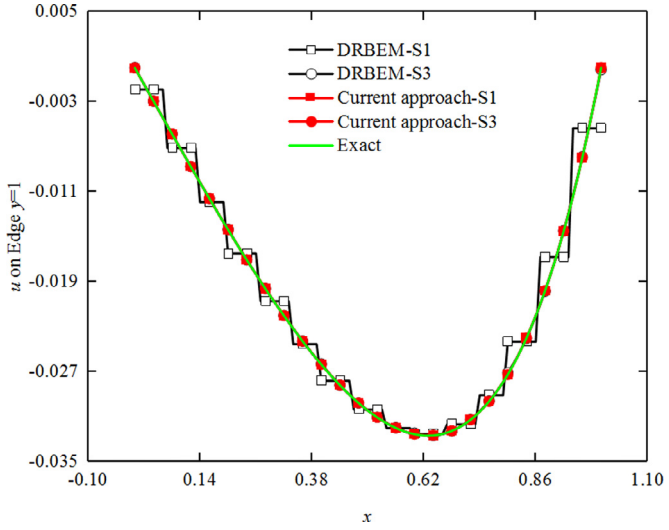

Fig. 11. Comparison of accuracy for u along the line y=1 in the second example.

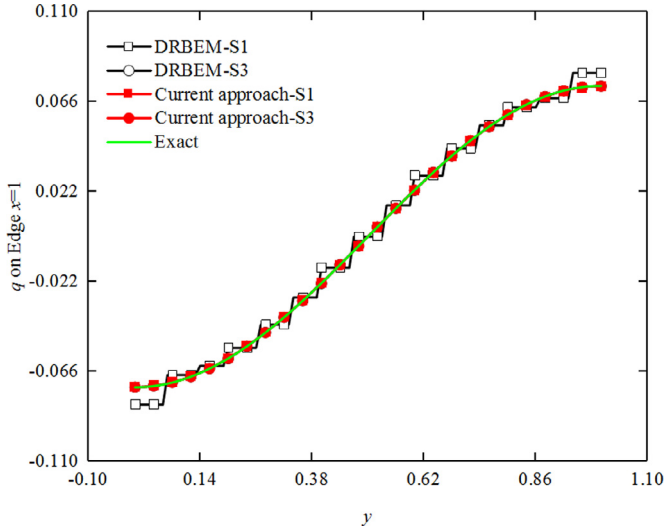

Fig. 12. Comparison of accuracy for q along the line x=0 in the second example.

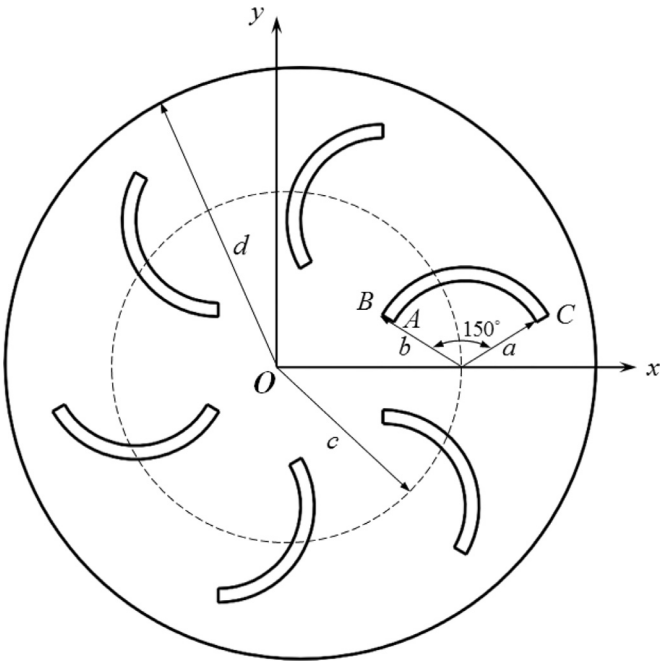

Fig. 13. Poisson equation on a complex structure with multiple short edges.

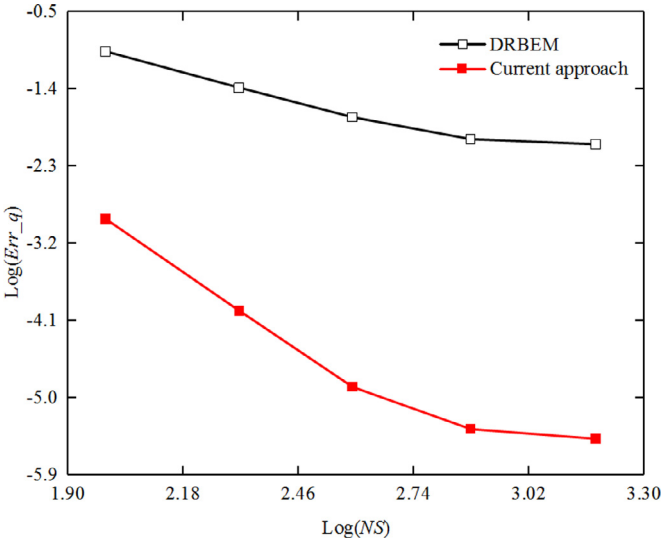

Fig. 14. Comparison of convergence for q in the third example.

where $\bar{\mathbf{u}}^s$, $\widehat{\mathbf{u}}^s$, $\bar{\mathbf{q}}^s$, and $\widehat{\mathbf{q}}^s$ are the known and unknown potentials and normal flux vectors for the source nodes, and $\bar{\mathbf{H}}^s$, $\widehat{\mathbf{H}}^s$, $\bar{\mathbf{G}}^s$, and $\widehat{\mathbf{G}}^s$ are the coefficient matrices, respectively. Eq. (33) describes a system of linear equations:

$$\mathbf{A}\mathbf{x} = \mathbf{b}, \tag{34}$$

in which

$$\mathbf{A} = \begin{Bmatrix} \widehat{\mathbf{H}}^s & \widehat{\mathbf{G}}^s \end{Bmatrix}, \ \mathbf{x} = \begin{Bmatrix} \widehat{\mathbf{u}}^s \\ \widehat{\mathbf{q}}^s \end{Bmatrix}, \ \mathbf{b} = \bar{\mathbf{G}}^s\bar{\mathbf{q}}^s - \bar{\mathbf{H}}^s\bar{\mathbf{u}}^s + \mathbf{b}_0,$$

where $\mathbf{A}$ is a $NS \times NS$ coefficient matrix, $\mathbf{x}$ is a $NS \times 1$ boundary vector of unknowns only for the source nodes, and $\mathbf{b}$ is a $NS \times 1$ known vector.

The size of Eq. (34) is identical to that in the traditional DRBEM with discontinuous elements, while the proposed method can achieve higher accuracy by improving the interpolation accuracy of boundary elements.

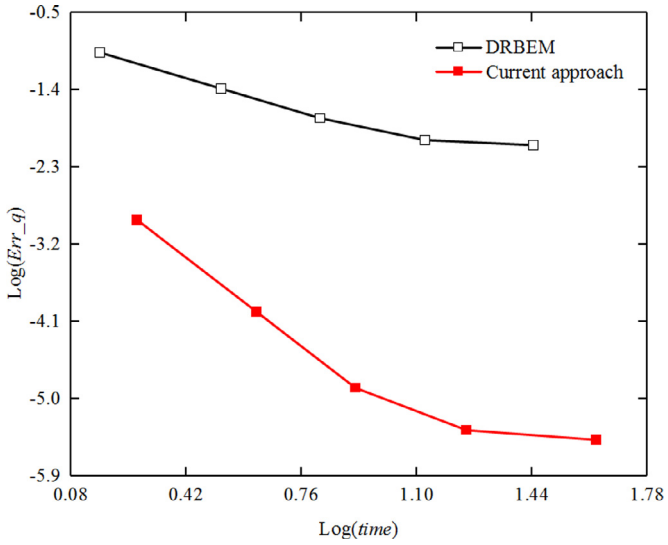

Fig. 15. Comparison of computational efficiency for q in the third example.

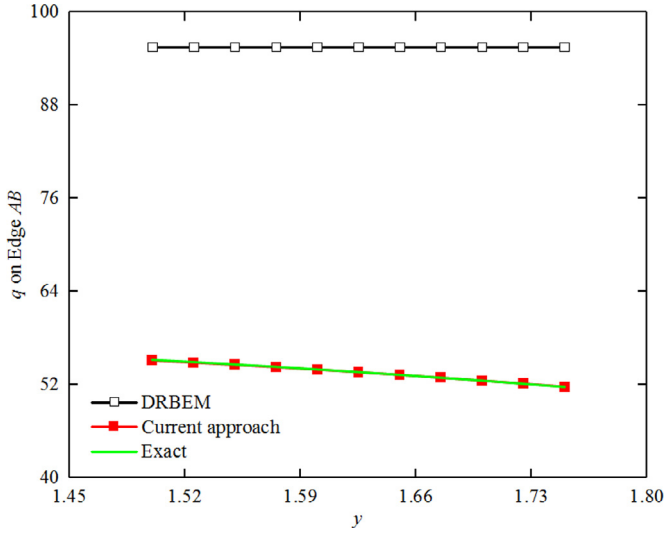

Fig. 16. Comparison of accuracy for q along the straight line AB in the third example.

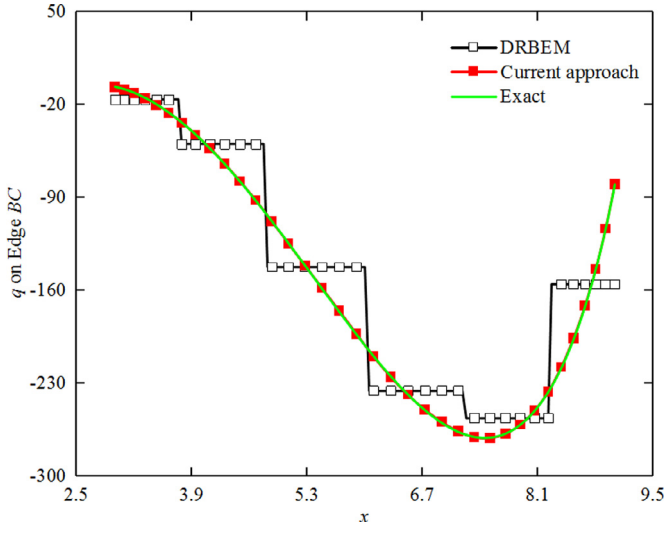

Fig. 17. Comparison of accuracy for q along the curve BC in the third example.

5. Numerical examples

Four numerical examples are used to illustrate the superiority of the proposed method for solving the Poisson equation. The earlier three examples which possess analytical solutions are given to testify the accuracy and efficiency of the presented method. The last practical numerical example is without analytical solution and designed to attest the practicability of current approach. Both the third and fourth examples highlight the advantages of our method to handle complex structures with small feature sizes.

The relative error is used to study error estimation and convergence of the proposed method and defined as follows:

$$error = \frac{1}{|v^{(e)}|_{\max}} \sqrt{\frac{1}{M}\sum_{i=1}^{M}\left[v_i^{(e)} - v_i^{(n)}\right]^2}, \tag{35}$$

where $|v^{(e)}|_{\max}$ is the maximum value of the exact solution over M sample points, and superscripts e and n denote the exact and numerical solutions, respectively. In the following numerical examples, the radial basis functions ATPS are employed in both conventional DRBEM and current approach. The symbols Err_u_B, Err_u_I and Err_q denote the relative errors for u of boundary nodes, internal nodes and q of boundary nodes, respectively. Furthermore, the symbols "DRBEM-S1" and "DRBEM-S3" denote conventional DRBEM with discontinuous constant and quadratic elements, "Current approach-S1" and "Current approach-S3" denote current approach with dual interpolation constant and quadratic elements, respectively.

5.1. Ellipse

The first example is the Poisson equation in the form of

$$\nabla^2 u = -x^2 \tag{36}$$

on the ellipse [6] depicted in Fig. 2 (a) with a semi-major axis $a = 2$ and a semi-minor axis $b = 1$, and u is the potential. The boundary condition $u = 0$ is specified along the boundary. The analytical solution of potential u corresponding to the above problem is given by:

$$u(x, y) = -\frac{1}{246}(50x^2 - 8y^2 + 33.6)\left(\frac{x^2}{4} + y^2 - 1\right), \tag{37}$$

which satisfies the Eq. (36) and boundary condition. The exact solution of normal flux q can be obtained by

$$q(x, y, n) = \frac{\partial u}{\partial x} n_x + \frac{\partial u}{\partial y} n_y, \tag{38}$$

where n_x and n_y are components of the outward normal of the boundary.

This simple example is given to attest the high accuracy and efficiency of the proposed method. The physical variables and particular solutions on the boundary are approximated by discontinuous constant and quadratic elements and in traditional DRBEM and dual interpolation S1and S3 elements in our method. Furthermore, 131 internal nodes are used as shown in Fig. 2 (b). With the increasing numbers of source points, Fig. 3 and 4 plot the convergence for Err_u_I and Err_q, Fig. 5 presents the computational efficiency of traditional DRBEM and our method, respectively. Furthermore, Fig. 6 shows the numerical and exact results of q along half of boundary with 60 source nodes and the abscissa is the angle θ shown in Fig. 2 (a).

As it may be observed from Fig. 3 to 5, when employing the same number of source points, the proposed method with dual interpolation S1 and S3 elements yields higher accuracy and efficiency than traditional DRBEM with discontinuous constant elements, and the formers process faster convergence rate than conventional DRBEM with discontinuous quadratic elements. Furthermore, the proposed method with S3 elements achieves higher efficiency than it with S1 elements. As a result, the proposed method attains higher accuracy and faster convergence rate than the traditional DRBEM. The reason is that the accuracy of interpolation for boundary physical variables and particular solutions in our method are higher than the traditional DRBEM.

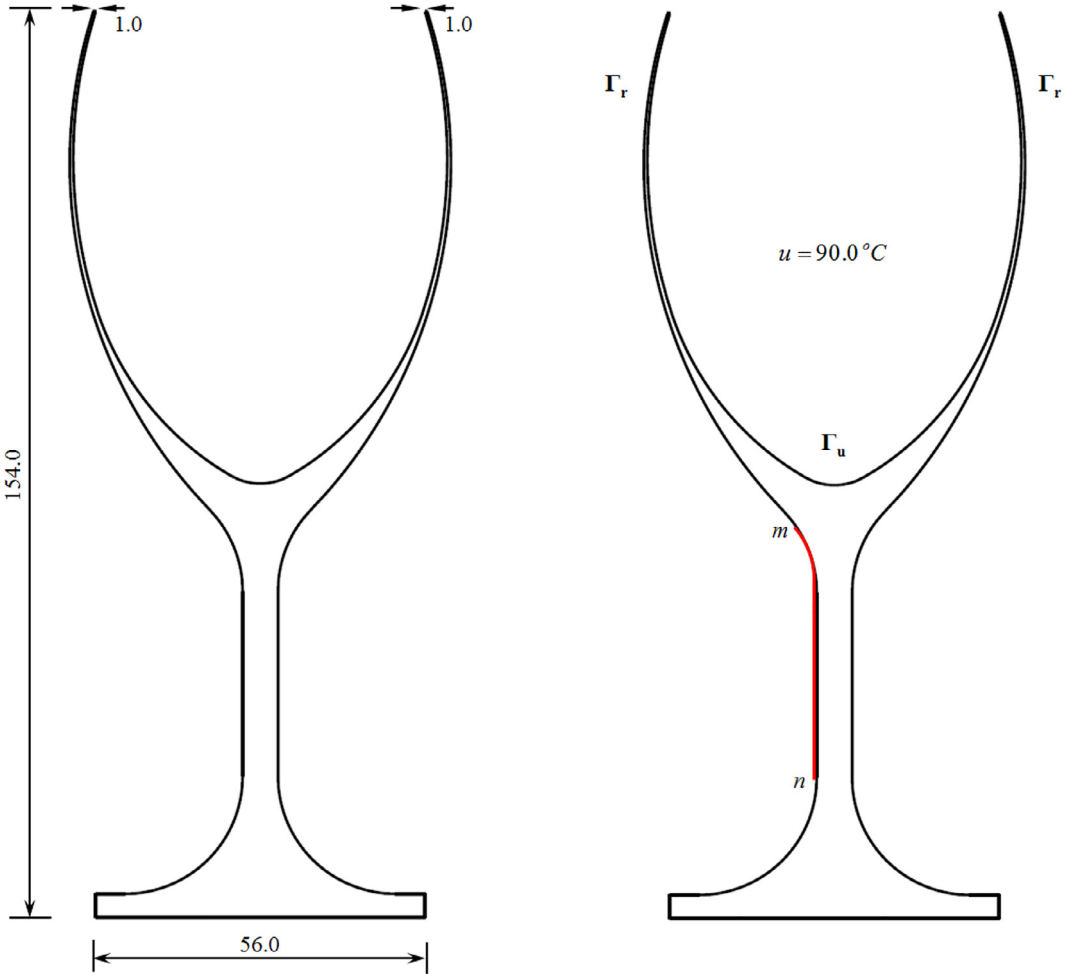

Fig. 18. Steady heat transfer problem of a goblet with thin walls.

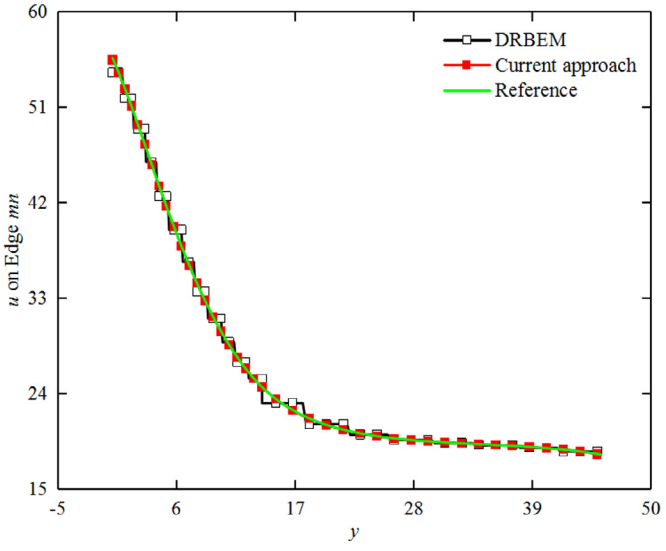

Fig. 19. Comparison of accuracy for u along the curve mn in the fourth example.

5.2. Square membrane

To testify the power of the proposed method to handle complex source term in the Poisson equation, a square membrane [10] subjected to variable domain force is analyzed. The size information is shown in Fig. 7 (a) and the domain force is $p(x, y) = \frac{x}{L}\cos\frac{\pi y}{L}$, so the governing equation is as follows:

$$\nabla^2 u = -\frac{x}{L}\cos\frac{\pi y}{L}. \tag{39}$$

Here, we choose L=1.0. In this problem, the boundary conditions are given by

$$\begin{cases} u = 0, \text{ for } x = 0 \text{ and } x = 1 \\ \frac{\partial u}{\partial n} = 0, \text{ for } y = 0 \text{ and } y = 1 \end{cases}. \tag{40}$$

The analytical solution for u can be found in [10], but it misses a minus "-". Thus, the exact solution is corrected into

$$u = -\left[\frac{L}{\pi^2 \sinh(\pi)}\sinh\frac{\pi x}{L} - \frac{x}{\pi^2}\right]\cos\frac{\pi y}{L}. \tag{41}$$

The exact normal derivative q is obtained by Eq. (38).

The physical variables and particular solutions on all edges are also approximated by constant and quadratic elements in two different methods, and 225 internal nodes are introduced as depicted in Fig. 7 (b). The relative errors for the boundary unknowns u_B and q are shown in Fig. 8 and 9, and the CPU time is plotted in Fig. 10, respectively. Moreover, the Fig. 11 and 12 present the comparisons of u and q along the lines y=1 and x=0 with 60 source nodes, respectively.

As shown in Fig. 8 to 12, the proposed method yields higher accuracy and faster convergence rate than the traditional DRBEM when using the same number of source points, for the same reason in the prior example.

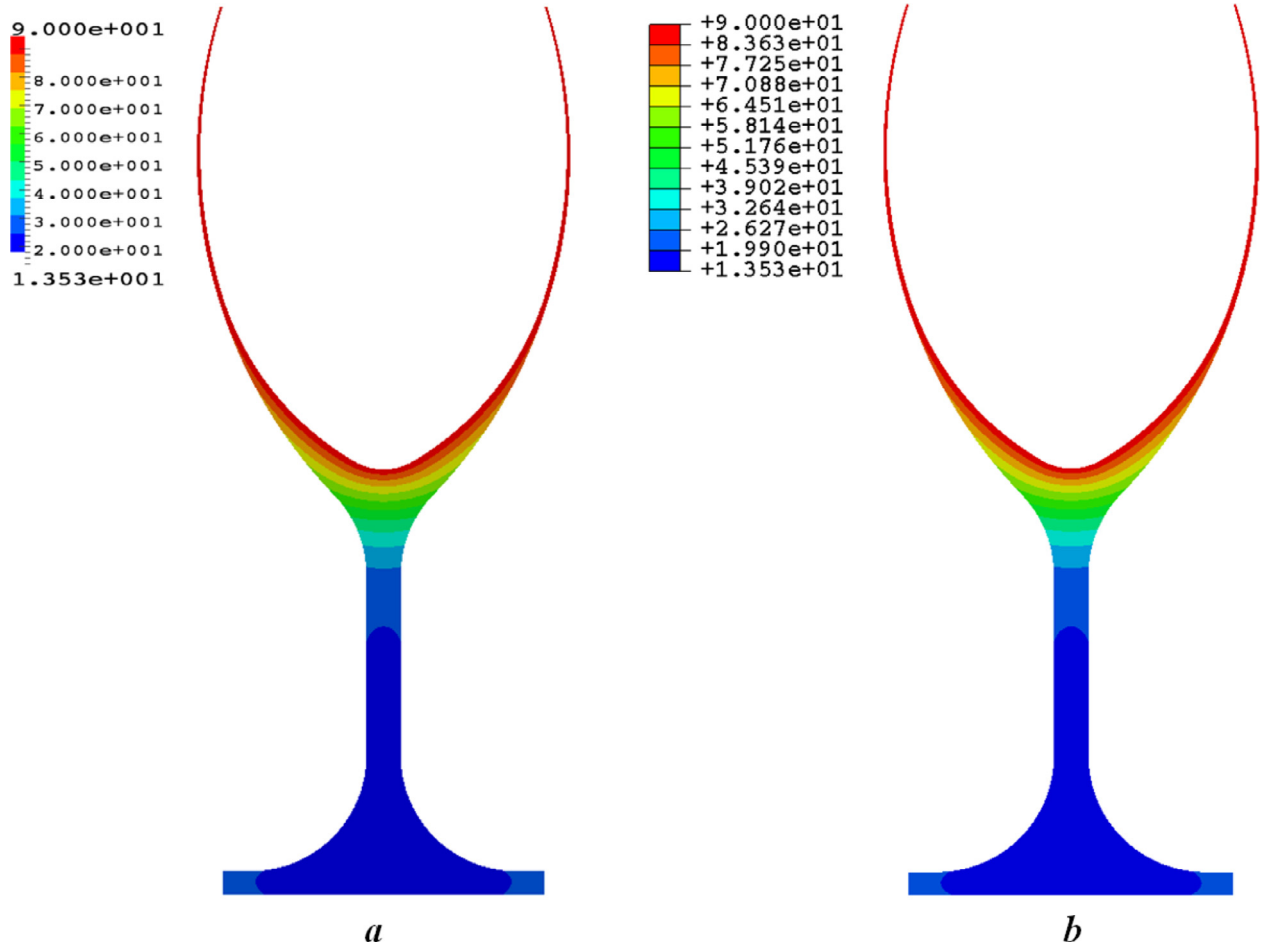

Fig. 20. Temperature distribution: (a) Current approach with 128 source points, (b) FEM with 464,362 nodes.

5.3. Complex structure with short edges

Our third example is the Poisson equation in the form of

$$\nabla^2 u = x + y \tag{42}$$

on a complex structure with multiple short edges shown in Fig. 13. The dimensions of this structure are given by a=3.0, b=3.5, c=6.0 and d=10.8. The Dirichlet boundary conditions are specified on all edges corresponding to the following analytical solution

$$u = -\frac{5}{6}\left(x^3 + y^3\right) + 3\left(x^2 y + x y^2\right) + 2(x - y), \tag{43}$$

This example is presented to highlight the superiority of the proposed method to handle complex structures even with small feature sizes. Constant elements are adopted to approximate the physical variables and particular solutions in two different numerical methods. In this example, there are two points that should be noted. First, the internal node is not necessary due to the ATPS approximation scheme is exact when the non-homogeneous term of the Poisson equation is a linear function. Second, only one source point is allocated on each of the short edges in Fig. 13.

Fig. 14 and 15 show the comparisons of accuracy and efficiency for traditional DRBEM and our method with the increasing numbers of source points on the boundary except the short edges, respectively. To demonstrate the higher accuracy of our method clearly, the normal flux q along the straight line AB and curve BC obtained by two numerical methods with 98 source nodes and the analytical solution are plotted in Fig. 16 and 17, respectively.

As observed between Fig. 14 and 17, the rate of convergence and accuracy of our method are visibly higher than those of conventional DRBEM. The main reason is that the interpolation accuracy of the S1 element on each short edge in our method increases by two orders compared with the constant element in traditional DRBEM. As a result, the q on the short edge AB is approximated exactly in our method as shown in **Fig. 16**. This example testifies the proposed method is clearly superior to conventional DRBEM when solving for complex structure with small feature sizes.

5.4. Steady heat transfer problem of a goblet with thin walls

Our last example is a steady heat transfer problem with unit heat source of a goblet filled with 90°C water as shown in Fig. 18, and the corresponding Poisson equation is as follows

$$\nabla^2 u = 1. \tag{44}$$

The sizes of this goblet and boundary conditions are shown in Fig. 18. Here, we chose a coefficient of heat conduction for the goblet of k=7.6 W/(m•K). The temperature of the inner faces Γ_u of the goblet is 90°C. The outside faces Γ_r of the goblet are exposed to the air. Thus, the convection boundary conditions (i.e., Robin boundary conditions) are considered as follows:

$$q = h(u - u_b), \tag{45}$$

where q and u are the heat flux and temperature on the outside faces, respectively, h is the convection coefficient, and ub is the ambient temperature. We chose h = 0.8 and ub = 23°C.

Similarly, all the physical variables and particular solutions are approximated by constant elements. Again, the internal node is not necessary and only one source point is allocated on each of the short edges in Fig. 18.

Here, we employ 128 source points in the conventional DRBEM and current approach. The reference solution is obtained by the Finite Element Method (FEM) with 464,362 nodes. Fig. 19 shows the results of temperature u along the red curve mn in Fig. 18. The temperature distribution in whole domain is shown in Fig. 20. As observed from Fig. 19 and 20, the numerical results obtained by current approach are indistinguishable from the reference solution, while the results from traditional DRBEM are inaccurate. This example highlights the superiority of our method to solve practical problem which is without exact solution.

6. Discussion and conclusions

In this paper, the DRM has been enhanced by coupling the dual interpolation boundary face method. In this new combined algorithm, the boundary physical variables and particular solutions are approximated by dual interpolation elements which improve the interpolation accuracy by two orders, compared with traditional discontinuous elements. Furthermore, we use ATPS as the radial basis function in the DRM for providing a non-singular interpolation matrix and exactly approximating the constant or linear function of the source term. Additionally, we employ the Hermite-type approximation as the second-layer interpolation because of its high accuracy and superiority to dispose structures with small feature sizes. As a result, compared with the conventional DRBEM, the proposed method can achieve higher accuracy and efficiency and is better suitable to solve for structures with small feature sizes. All presented numerical examples demonstrate the accuracy and efficiency of our method, when it solves Poisson equation with different types of boundary condition.

We just study the performance of the proposed method, when it applies to two-dimensional Poisson equation. In future work, we plan to extend the range of applicability of the method to the three-dimensional case and other non-homogeneous partial differential equations.

Declaration of Competing Interest

None.

Acknowledgments

This work was supported by National Natural Science Foundation of China under grant numbers 11772125 and 11972010. We also express thanks to anonymous referees whose comments significantly improved the paper.

References

[1] Wen PH, Aliabadi MH, Rooke DP. Cracks in three dimensions: A dynamic dual boundary element analysis. Comput Methods Appl Mech Eng 1998;167:139–51.
[2] Cheng AD, Chen CS, Golberg MA, Rashed YF. BEM for theomoelasticity and elasticity with body force-a revisit. Eng Anal Bound Elem 2001;25:377–87.
[3] Yao ZH, Kong FZ, Wang HT, Wang PB. 2D simulation of composite materials using BEM. Eng Anal Bound Elem 2004;28:927–35.
[4] Liu YJ, Nishimura N. The fast multipole boundary element method for potential problems: a tutorial. Eng Anal Bound Elem 2006;30:371–81.
[5] Zhang YM, Gu Y, Chen JT. Stress analysis for multilayered coating systems using semi-analytical BEM with geometric non-linearities. Comput Mech 2011;47:493–504.
[6] Partridge PW, Brebbia CA, Wrobel LC. The dual reciprocity boundary element method. Southampton: Computational Mechanics Publications; 1992.
[7] Nardini D, Brebbia CA. A new approach to free vibration analysis using boundary elements. Appl Math Modell 1983;7:157–62.
[8] Loeffler CF, Mansur WJ. Analysis of time integration schemes for boundary element applications to transient wave propagation problems. In: Brebbia CA, editor. Boundary element techniques: applications in stress analysis and heat transfer. UK: Computational Mechanics Publishing; 1987. p. 105–24.
[9] Bui TT, Popov V. Domain decomposition boundary element method with overlapping sub-domains. Eng Anal Bound Elem 2009;33:456–66.
[10] Loeffler CF, Cruz AL, Bulcão A. Direct use of radial basis interpolation functions for modelling source terms with the boundary element method. Eng Anal Bound Elem 2015;50:97–108.
[11] Golberg MA, Chen CS. The theory of radial basis functions applied to the BEM for inhomogeneous partial differential equations. Bound Elem Commun 1994;5:57–61.
[12] Golberg MA, Chen CS, Karur SR. Improved multiquadric approximation for partial differential equations. Eng Anal Bound Elem 1996;18:9–17.
[13] Karur SR, Ramachandran PA. Augmented thin plate spline approximation in DRM. Bound Elem Commun 1995;6:55–8.
[14] Yamada T, Wrobel LC, Power H. On the convergence of the dual reciprocity boundary element method. Eng Anal Bound Elem 1994;13:291–8.
[15] Chen CS, Golberg MA, Schaback R. Recent developments in the dual reciprocity method using compactly supported radial basis functions. Transf Domain Effect Bound 2003;1:1–41.
[16] Wendland H. Piecewise polynomial, positive definite and compactly supported radial functions of minimal degree. Adv Comput Math 1995;4:389–96.
[17] Zhang JM, Han L, Lin WC, Dong YQ, Ju CM. A new implementation of BEM by an expanding element interpolation method. Eng Anal Bound Elem 2017;78:1–7.
[18] Zhang JM, Lin WC, Dong YQ, Ju CM. A double-layer interpolation method for implementation of BEM analysis of problems in potential theory. Appl Math Modell 2017;51:250–69.
[19] Zhang JM, Dong YQ, Lin WC, Ju CM. A singular element based on dual interpolation BFM for V-shaped notches. Appl Math Modell 2019;71:208–22.
[20] Zhang JM, He R, Chi BT, Lin WC. A dual interpolation boundary face method with Hermite-type approximation for potential problems. Appl Math Modell 2020;81:457–72.
[21] Zhang JM, He R, Lin WC, Yang L, Chi BT, Suliman. A dual interpolation boundary face method with Hermite-type approximation for elasticity problems. Eur J Mech-A/Solids 2020;82:104005.
[22] Qin XY, Zhang JM, Li GY, Sheng XM, Song Q, Mu DH. An element implementation of the boundary face method for 3D potential problems. Eng Anal Bound Elem 2010;34:934–43.
[23] Li G, Aluru NR. Boundary cloud method: a combined scattered point/boundary integral approach for boundary-only analysis. Comput. Methods Appl Mech Eng 2002;91:2337–70.